

DOI: 10.1002/adem.((please add manuscript number))

Manufacturing and Characterization of Highly Porous Bioactive Glass Composite Scaffolds using Unidirectional Freeze Casting**

By *Laura M. Henning*[§], *Sara Zavareh*[§], *Paul H. Kamm*, *Miriam Höner*, *Horst Fischer*, *John Banhart*, *Franziska Schmidt*^{*}, and *Aleksander Gurlo*

[*] *Dr. F. Schmidt (corresponding author), L. M. Henning, S. Zavareh, Prof. Dr. A. Gurlo Technische Universität Berlin, Institut für Werkstoffwissenschaften und -technologien, Fachgebiet Keramische Werkstoffe / Chair of Advanced Ceramic Materials Hardenbergstr. 40, Berlin, 10623, Germany*

E-mail: franziska.schmidt@ceramics.tu-berlin.de

Prof. Dr. J. Banhart, P. H. Kamm

Helmholtz-Zentrum Berlin für Materialien und Energie, Institut für Angewandte Materialforschung / Institute of Applied Materials

Hahn-Meitner-Platz 1, Berlin, 14109, Germany

Prof. Dr. H. Fischer, M. Höner

Universitätsklinikum RWTH Aachen, Zahnärztliche Werkstoffkunde und Biomaterialforschung / Dental Materials and Biomaterials Research

Pauwelsstr. 30, Aachen, 52074, Germany

[**] *We thank Clemens Randow and Prof. Claudia Fleck from TU Berlin, Institut für Werkstoffwissenschaften und -technologien, Fachgebiet Werkstofftechnik, for their help provided in testing the mechanical properties. The financial support by the internal research funding program of the Technische Universität Berlin is greatly acknowledged.*

[[§]] *Authors with equal contribution*

The aim of this work is the fabrication of bioactive and degradable scaffolds for bone tissue engineering. Freeze casting is used to obtain macropores. Alongside highly bioactive 45S5 Bioglass, gelatin and chitosan are used as biocompatible binder and stabilizing agent, respectively. By varying the cooling rate between 2 and 4 K/min and whether the slurry was allowed to form a gelled network at 7 °C before freeze casting or not, samples with porosities of 75 % are achieved. X-ray tomography analysis shows smallest pore sizes between 73 and 77 μm and a rather lamellar structure parallel to the freezing direction for the non-gelled samples, whereas the gelled samples have smallest pores between 96 and 120 μm and show a rather cellular structure. Compression tests reveal compressive strengths from 2 MPa (non-gelled) to 3 MPa (gelled), while the quasielastic moduli of the gelled samples (44-46 MPa)

1
2
3
4
5
6
7
8
9
10
11
12
13
14
15
16
17
18
19
20
21
22
23
24
25
26
27
28
29
30
31
32
33
34
35
36
37
38
39
40
41
42
43
44
45
46
47
48
49
50
51
52
53
54
55
56
57
58
59
60
61
62
63
64
65

clearly exceed values of the non-gelled (20-23 MPa). Thus, it was concluded that the modified pore structure caused by the gelling process markedly improves the mechanical properties of the samples. After seven days in SBF under physiological conditions, a calcium phosphate rich layer was detected on the samples surface, revealing the bioactivity of the scaffolds.

1. Introduction

In recent years, combining bioactive and degradable materials has received great interest in tissue engineering. During their degradation, the contained bioactive components induce a stimulation resulting in the regeneration of tissue^[1-5]. While inert materials are only tolerated by the human body and may lead to the formation of connective tissue surrounding the material, bioactive materials elicit a specific biological response at the interface between the material and the human body leading to a bond between the scaffold and the remaining bone^[4-8]. 45S5 Bioglass (45 SiO₂, 24.5 Na₂O, 24.5 CaO, 6 P₂O₅ wt.%), developed in 1969 by Larry Hench, has the highest bioactivity and fastest bonding rate to soft and hard tissue^[9,10]. It is commercially available, inexpensive, and can be acquired in high purity^[11]. Hence, 45S5 Bioglass^[12-17] has been investigated in several studies for scaffold applications in tissue engineering. Besides adequate mechanical properties and surface roughness^[18-20], a highly porous structure and a sufficient pore size range are particularly important requirements in order to enable interactions between the cells and the scaffold^[20-22]. Such a porous structure can be generated by different techniques, including robotic deposition^[23,24], gel casting^[25], microsphere leaching^[26], and layer casting combined with lamination^[27]. Furthermore, different techniques for fabricating hierarchical porosity, e.g. the sol-gel process, are applied^[28].

The main goal of the present study is to fabricate bioactive macroporous scaffolds by freeze casting of a Bioglass slurry formulated with biocompatible additives such as gelatin and chitosan and to characterize the bioactivity of the scaffolds in a dynamic bioactivity reactor in

1 simulated body fluid (SBF). We combined gel casting and freeze casting to ensure a stable
2 network of open, well interconnected pores suitable for the transport of nutrients and
3
4 metabolites since gel casting on its own leads to poorly connected pores^[25].
5
6

7 Freeze casting, also referred to as ice templating, is one of the most promising techniques to
8
9 fabricate bio-inspired macroporous composites with interconnected pores^[29–35]. In this
10
11 technique, a suspension, most commonly aqueous, is frozen under controlled conditions,
12
13 followed by the formation of pores during the sublimation of ice by freeze drying. As this
14
15 technique is relatively easy to apply and is environmentally friendly, it is a good candidate for
16
17 the production of porous scaffolds for tissue engineering applications. Bioactive
18
19 glass/biopolymer composites are widely investigated for mimicking bone tissue^[26,27,36–39].
20
21

22
23 When applying the freeze casting technique a binder, usually a biopolymer, is needed to
24
25 achieve adequate cohesion after the freeze-drying process and improve the mechanical
26
27 properties of the green body^[26]. Gelatin is a natural protein complex derived from collagen. It
28
29 is inexpensive, commercially available, degradable, and contains Arg-Gly-Asp (RGD)-like
30
31 sequences, which can promote cell adhesion and migration^[37]. Therefore it is a good choice
32
33 when considering biocompatible binders for bio-inspired applications^[40]. Chitosan^[41,42], a
34
35 degradable biopolymer, forms an electrolyte complex when combined with gelatin and thus
36
37 increases cell compatibility, cell proliferation and decreases apoptosis^[43,44].
38
39
40
41
42

43 We are the first group fabricating highly interconnected porous scaffolds using commercial
44
45 45S5 Bioglass, gelatin and chitosan via freeze casting and combined gel casting and freeze
46
47 casting, respectively. The biopolymer addition allows the achievement of high stability in the
48
49 porous scaffolds in the green state without use of a crosslinking agent which reduces the
50
51 necessity for further processing. In contrast to sintering, which induces structural
52
53 transformations and results in at least partial crystallinity^[45], the original composition and the
54
55 amorphous structure of the Bioglass can be preserved.
56
57
58
59
60
61
62
63
64
65

2. Materials and Methods

The experimental procedure for fabricating the porous scaffolds is illustrated in **Figure 1**.

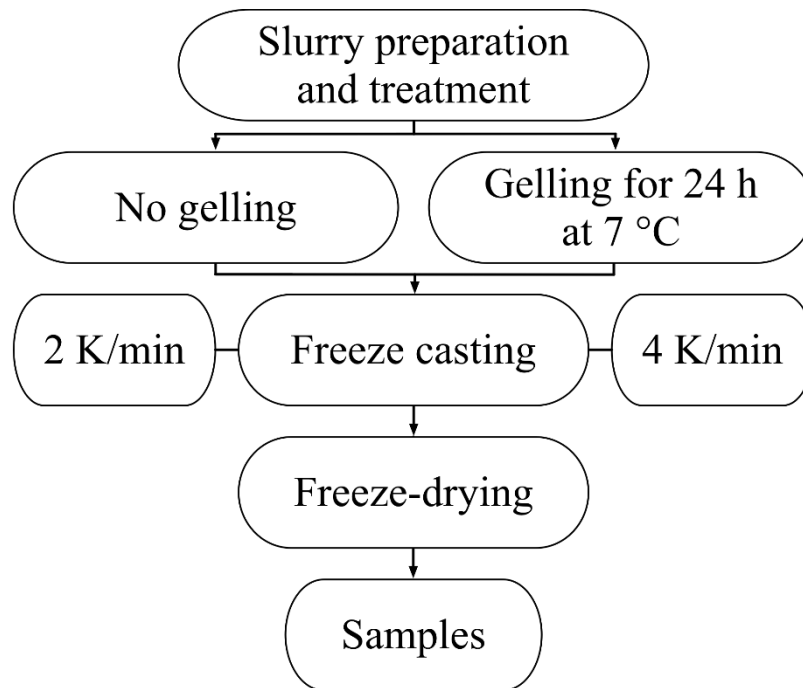


Figure 1. Scheme depicting the experimental procedure for the scaffold production

2.1. Preparation of the Slurry

For the preparation of the aqueous slurry consisting of 71.5 wt.% 0.5 M acetic acid solution, 26 wt.% Bioglass, 1.5 wt.% gelatin, 0.7 wt.% chitosan and 0.3 wt. % polydimethylsiloxane (PDMS) the following steps were performed. Chitosan (Mw ~ 15 000, degree of acetylation > 85 %, Polysciences Inc., Germany) was dissolved in 0.5 M acetic acid (diluted from acetic acid 100 %, Merck, Germany) under stirring for 18 h at room temperature. Afterwards, gelatin (from porcine skin, 180 g bloom, Sigma-Aldrich, Germany) was added to the solution as a binder and dissolved at 60 °C in an ultrasonic bath (Bandelin Sonorex RK 514 H) for 30 min. Then polydimethylsiloxane (PDMS, silicone oil M 50, Carl Roth, Germany) as a defoaming agent and commercially available Bioglass powder (Vitryxx®, $d_{50} = 4.0 \pm 1.0 \mu\text{m}$, Schott, Germany) were added to the solution. The resulting slurry was then treated with an ultrasonic finger (Branson Sonifier 450) and degassed under vacuum.

2.2. Preparation of Bioactive Glass Scaffolds

1
2 One half of the as-prepared slurry was freeze casted directly (not gelled, NG) in a self-made
3
4 setup^[46] in cylindrical molds made of acrylic glass ($\varnothing = 10$ mm, height = 20 mm, in-house
5
6 production) and subsequently freeze-dried in a commercial freeze-dryer (Christ Gamma 2-20,
7
8 Martin Christ Gefriertrocknungsanlagen GmbH, Germany) for 116 h at 20 °C and 0.03 mbar.
9
10 The other half of the slurry was gelled (G) beforehand by refrigeration for 24 h at 7 °C,
11
12 followed by freeze casting and freeze-drying as described above. Two different cooling rates,
13
14 namely 2 K/min and 4 K/min, were chosen for the controlled freezing of the slurry.
15
16 Altogether, four different samples were obtained by varying the cooling rate and whether the
17
18 slurry was gelled beforehand or not (i.e. NG 2 K/min, NG 4 K/min, G 2 K/min and
19
20 G 4 K/min).
21
22
23
24
25
26
27
28

2.3. Characterization methods

2.3.1. Particle Size Analysis

29
30
31 The particle size distributions of the as-delivered Bioglass and of the as-prepared slurry were
32
33 determined using a Helos H1505 laser diffraction analyzer with a SuceLL dispersion system
34
35 (Sympatec, Germany). The measuring range was 0.5-175 μm , the optical density 5 % and the
36
37 measurement conditions 10 s reference measurement, 10 s normal measurement and 60 s
38
39 ultrasonic dispersion at 60% stirring intensity. Three measurements were performed for each
40
41 sample in order to ascertain reproducibility of the results.
42
43
44
45
46
47
48
49
50
51
52
53
54
55

2.3.2. Rheological Analysis

1
2 Viscosity measurements were performed using a Physica MCR 301 rotary rheometer (Anton
3 Paar, Germany) in a plate-plate setup with the measuring system PP50 and a gap size of
4 0.5 mm at 25 °C.
5
6
7
8

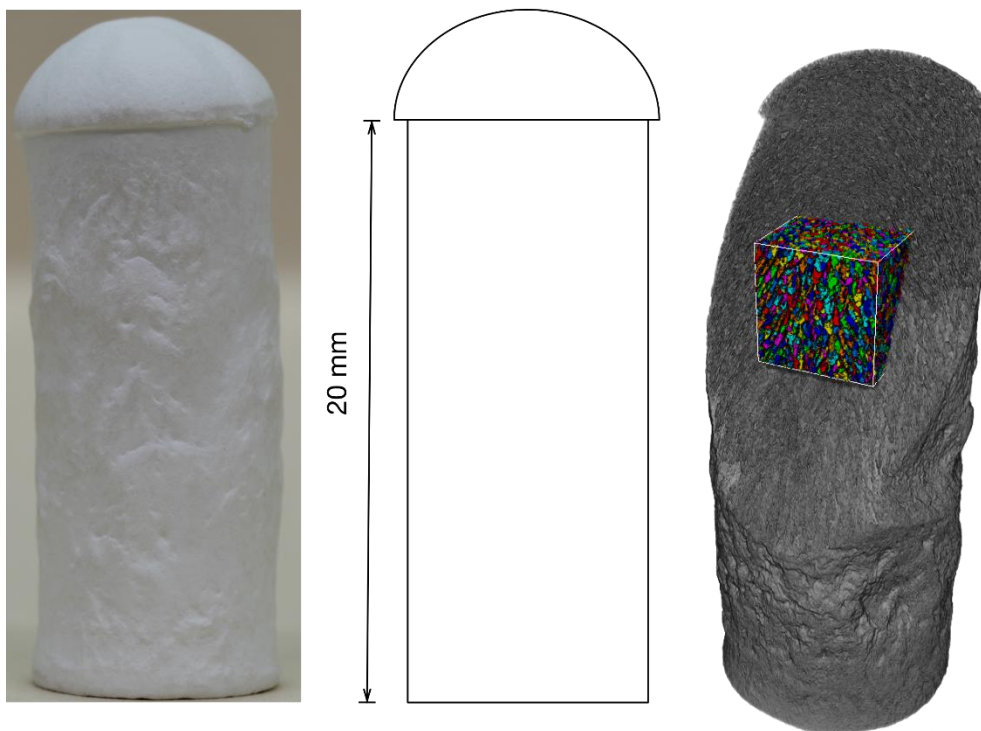
9 2.3.3. Porosity Calculation

10 The total porosity ϕ of the specimens was calculated according to

$$14 \phi = 1 - \frac{\rho_r}{\rho} \times 100 [\%], \quad (1)$$

17 where the solid density ρ was calculated from the mass of the specimen and its volume
18 determined by a Multivolume Pycnometer 1305 helium pycnometry (Micromeritics
19 Instrument Corporation, USA). The raw density ρ_r was calculated from the mass of the
20 specimen and its volume, which was herein approximated by a cylinder and a hemisphere, see
21
22
23
24
25
26

27 **Figure 2.**



54
55 Figure 2. From left to right: Typical image of a sample, schematic for the geometrical
56 approximation, X-ray tomography reconstruction (G 2 K/min) showing the analyzed volume.
57
58
59

60 2.3.4. Scanning Electron Microscopy (SEM)

1 The microstructure of the scaffold surfaces was characterized by means of a S520 scanning
2 electron microscope (Hitachi, Japan). The specimens were obtained by controlled cut-off
3 followed by breaking of the scaffolds. The obtained surfaces were characterized in terms of
4 topography and pore size.
5
6
7
8
9

10 11 2.3.5. X-ray Tomography

12 To obtain information about the size and orientation of the pores in the scaffolds, X-ray
13 tomography measurements were conducted in a home-made setup^[47]. The setup consists of a
14 C7942CA-02 flat panel detector (Hamamatsu, Japan) and a L8121-03 microfocus X-ray tube
15 (Hamamatsu, Japan), which was operated at 60 kV. The magnification was adjusted to a
16 resulting image resolution of 12 μm pixel size. Tomographic reconstructions were computed
17 using Octopus 8, while Avizo 9 was used to generate 3D reconstructions from the cross
18 sections and to analyze the data. In order to reduce computational cost and time, only data
19 within a cube with an edge length of 4 mm were analyzed for each sample. The position of
20 the analyzed volume is mapped in Figure 2. Starting from filtered, binarized gray images, the
21 pores were segmented by application of the watershed transformation with a Chamfer
22 distance transformation. Pores with a volume of less than 60 voxels were excluded, as they
23 can be attributed to background noise. The following parameters of the pores were analyzed:
24 (i) the extent of the data in the direction of the shortest pore axis, meaning the channel
25 thickness of the pores and (ii) the angle between the longest pore axis and the freezing
26 direction.
27
28
29
30
31
32
33
34
35
36
37
38
39
40
41
42
43
44
45
46
47
48
49
50
51
52

53 2.3.6. Mechanical Properties

54 To investigate the stress-strain behavior of the scaffolds, a micro tensile compression tester
55 (Kammrath & Weiss, Germany) with a LVDT (Linear Variable Differential Transformer)
56 sensor, a 500 N load cell, and the microprocessor control DDS 32 was used. Compression
57
58
59
60
61
62
63
64
65

1 tests were conducted with a test speed of $5 \mu\text{m s}^{-1}$ until up to 450 N. Discoidal specimens with
2 a thickness of 2 mm were cut from underneath the hemispherical top of the sample using a
3
4 Buehler Isomet 2000 saw with a MOD08 diamond cut-off wheel (Struers, Germany). Up to
5
6 three specimens were tested for each kind of sample.
7
8
9

10 11 2.3.7. Bioactivity Test

12 To test the in vitro bioactivity of the specimens, two samples NG 4 K/min, beforehand
13
14 thermally treated for 24 h at $110 \text{ }^\circ\text{C}$, were placed in an SBF reactor under physiological flow
15
16 conditions as reported previously^[48]. The samples were placed in a PVC reactor chamber
17
18 under constant SBF flow of $3 \mu\text{m s}^{-1}$ at the sample surfaces. The experiment was carried out
19
20 for seven days at $37 \text{ }^\circ\text{C}$. Afterwards, the samples were removed from the solution, carefully
21
22 dipped into deionized water, and dried in a desiccator. The surface reaction layers were
23
24 analyzed by a XL30 field emission scanning electron microscope (FEI/Philips, The
25
26 Netherlands) and Falcon energy dispersive X-ray spectroscopy with Genesis EDS software
27
28 (EDAX, USA).
29
30
31
32
33
34
35
36
37
38

39 3. Results and Discussion

40 41 3.1. Particle Size Distribution and Rheological Properties of the Slurry

42
43 **Figure 3** shows the particle size distribution (i.e. the medians of three measurements) of the
44
45 prepared slurry and the as-delivered Bioglass powder. For the slurry, characteristic particle
46
47 sizes are $d_{50} = 5.4 \mu\text{m}$ and $d_{90} = 15.8 \mu\text{m}$, while they are $d_{50} = 3.9 \mu\text{m}$ and $d_{90} = 8.7 \mu\text{m}$ for the
48
49 Bioglass. The slight increase in the particle size for the slurry is caused by the formation of
50
51 agglomerates due to the polymer addition.
52
53
54
55
56
57
58
59
60
61
62
63
64
65

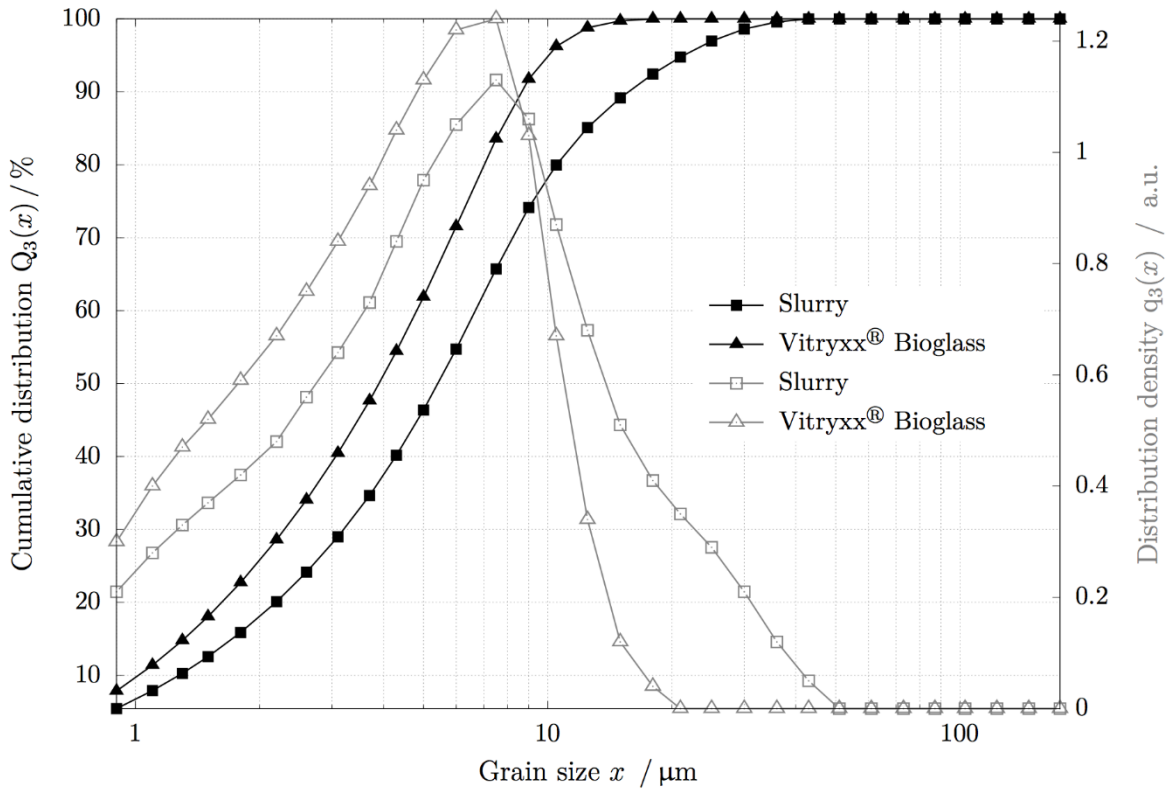


Figure 3. The particle size distribution of the Bioglass powder and the prepared slurry. Black/filled symbols and gray/hollow symbols illustrate the cumulative distribution and distribution density over particle size, respectively.

The results of the rheological analysis are shown in **Figure 4**. The dynamic viscosity decreased with increasing shear rate, meaning the slurry showed a shear-thinning behavior which is very suitable for casting. An absence of hysteresis indicates no sedimentation during the measurement which in turn confirms the stability of the slurry.

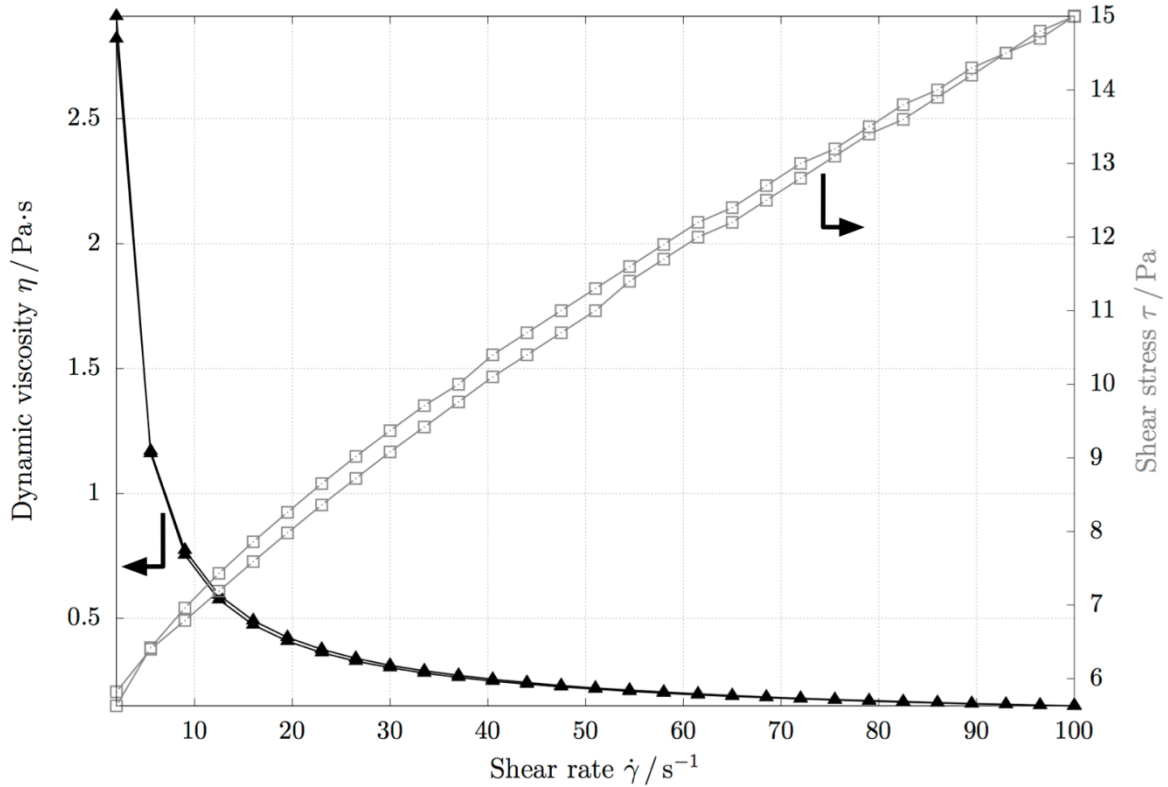


Figure 4. The dynamic viscosity of the slurry decreases with an increasing shear rate confirming the shear-thinning behavior of the slurry. Black/filled symbols and gray/hollow symbols illustrate the dynamic viscosity and shear stress over shear rate, respectively.

3.2. Microstructure and Porosity of the Scaffolds

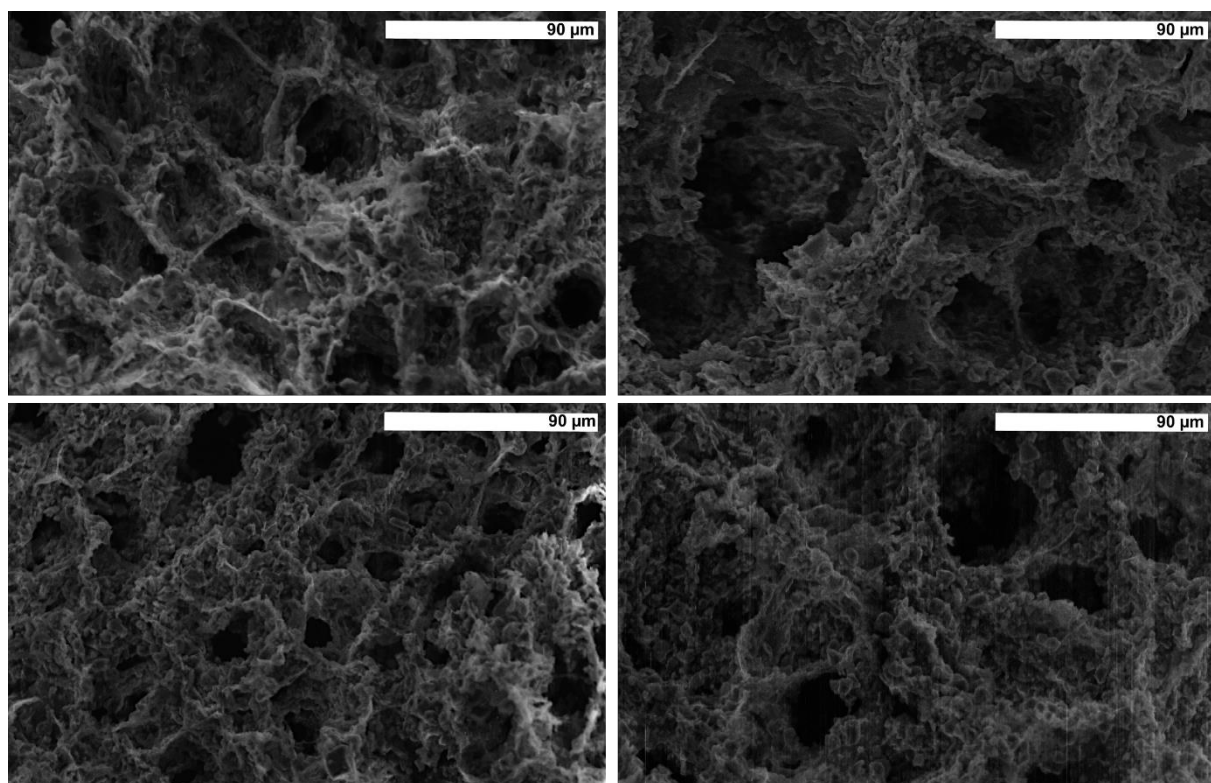
Table 1. Solid densities, raw densities and calculated porosities of all specimens.

	NG 2 K/min	NG 4 K/min	G 2 K/min	G 4 K/min	$\bar{\phi} \pm \text{SD}$
Solid density [g cm^{-3}]	2.25	2.27	2.18	2.22	2.23 ± 0.03
Raw density [g cm^{-3}]	0.58	0.53	0.55	0.54	0.55 ± 0.02
Porosity [%] acc. Eq. 1	74.36	76.82	74.65	75.87	75.43 ± 1.0

Table 1 shows the solid densities, raw densities and calculated porosities for all specimens as well as the associated averages and standard deviations (SD). Because the same slurry composition was used for all samples, the densities were very similar for all samples. Due to the biopolymer addition, the solid density is lowered from 2.7 g cm^{-3} , the density of 45S5 Bioglass^[49], to 2.23 g cm^{-3} in average. The weight reduction is beneficial when mimicking the

1 lightweight structure of human bone^[50]. Given by the process, the total porosity of 75 % in
2 average was open, so that in theory there is no restriction for the transport of nutrients and
3
4 metabolites. **Figure 5** displays the surface microstructure of the prepared specimens. The
5
6 micrographs show predominantly cellular structures with different pore sizes. As shown in
7
8 Figure 5, the samples frozen with a cooling rate of 2 K/min (top row) illustrate larger pores
9
10 compared to the samples frozen with a cooling rate of 4 K/min. The micrographs also indicate
11
12 that the gelation process (right column in Figure 5) causes larger pores when compared to the
13
14 non-gelled samples (left column in Figure 5).
15
16

17
18 In addition, the microstructure of the specimens in Figure 5 indicates a sufficient surface
19
20 roughness for successful cell adhesion and proliferation. In contrast to smooth surfaces, which
21
22 impede cell adhesion and promote inflammation, cells can anchor at textured surfaces^[51].
23
24
25



53
54 Figure 5. SEM micrographs of the prepared scaffolds. Top left: NG 2 K/min, bottom left:
55 NG 4 K/min, top right: G 2 K/min, bottom right: G 4 K/min. Scale bar is 90 μm .
56

57
58 In order to obtain more information about the size and orientation of the pores, the scaffolds
59
60 were characterized by X-ray tomography. **Figure 6** shows X-ray tomographic xy- and xz-
61
62
63

1 cross sections which allow the analysis of the pore structures of the four different samples. As
2 shown in Figure 6 (xz- cross section), a very light gray area can be found at the bottom,
3
4 indicating very narrow and small pores due to the planar ice crystal growth during initial
5
6 freezing. In the first stage of solidification randomly oriented ice nuclei were generated. Ice
7
8 nucleation is a thermodynamic process and occurs very fast due to the large supercooling of
9
10 the suspension which entraps the Bioglass particles.^[29] After the nucleation stage, the ice
11
12 crystals grew and the planar structure changed into a lamellar structure. During growth the
13
14 Bioglass particles were rejected from the ice crystals and capsulated, thus forming the walls
15
16 of the scaffolds. Due to the fact that the lamellae growth strongly depends on rheological
17
18 properties of the suspension and the cooling conditions, the ice crystal growth is interrupted
19
20 by the growth of other ice crystal lamellae with new orientations. This leads to a cellular
21
22 structure.
23
24
25
26
27

28 For the G samples, the ice crystal growth was limited by the previously formed gelatin
29
30 network. Therefore, stronger repulsive forces were needed for generating the well-aligned
31
32 lamellae.^[34] The results of the X-ray tomography analysis for the shortest pore axis are listed
33
34 in **Table 2**. The average values of the shortest distance for the G samples are significantly
35
36 higher ($> 96 \mu\text{m}$) than for the NG samples ($> 72 \mu\text{m}$). This indicates wider pore channels in
37
38 the G samples, than in the NG samples. Furthermore, samples solidified with a cooling rate of
39
40 4 K/min possess smaller pores than the ones frozen at 2 K/min cooling rate. Higher cooling
41
42 rates bring about briefer ice crystal growth, thereby the cooling rate directly influences the
43
44 resulting ice crystal size and the pore structure formed^[29]. As the shortest distance was found
45
46 to exceed $70 \mu\text{m}$ on average and consequently the other axes are larger, the targeted
47
48 requirements for the pore size of the scaffold^[21] could be met. The relatively high standard
49
50 deviations provide a wide range of pore sizes so that tasks like enabling cell ingrowth and
51
52 regeneration of bone can be coped with. The angle between the longest pore axis and the
53
54 freezing direction is depicted in **Figure 7**. Dark blue colored pores have grown close to the
55
56
57
58
59
60
61
62
63
64
65

freezing direction, which corresponds to an angle of 0° , red colored pores show deviations up to 55° from the freezing direction. While the pores of the NG samples have clearly grown with the freezing direction, the pores of the G samples show bigger deviations to the freezing direction. This can be explained by the gelatin network generated in the G samples that hinders growth of lamellae parallel to the freezing direction.

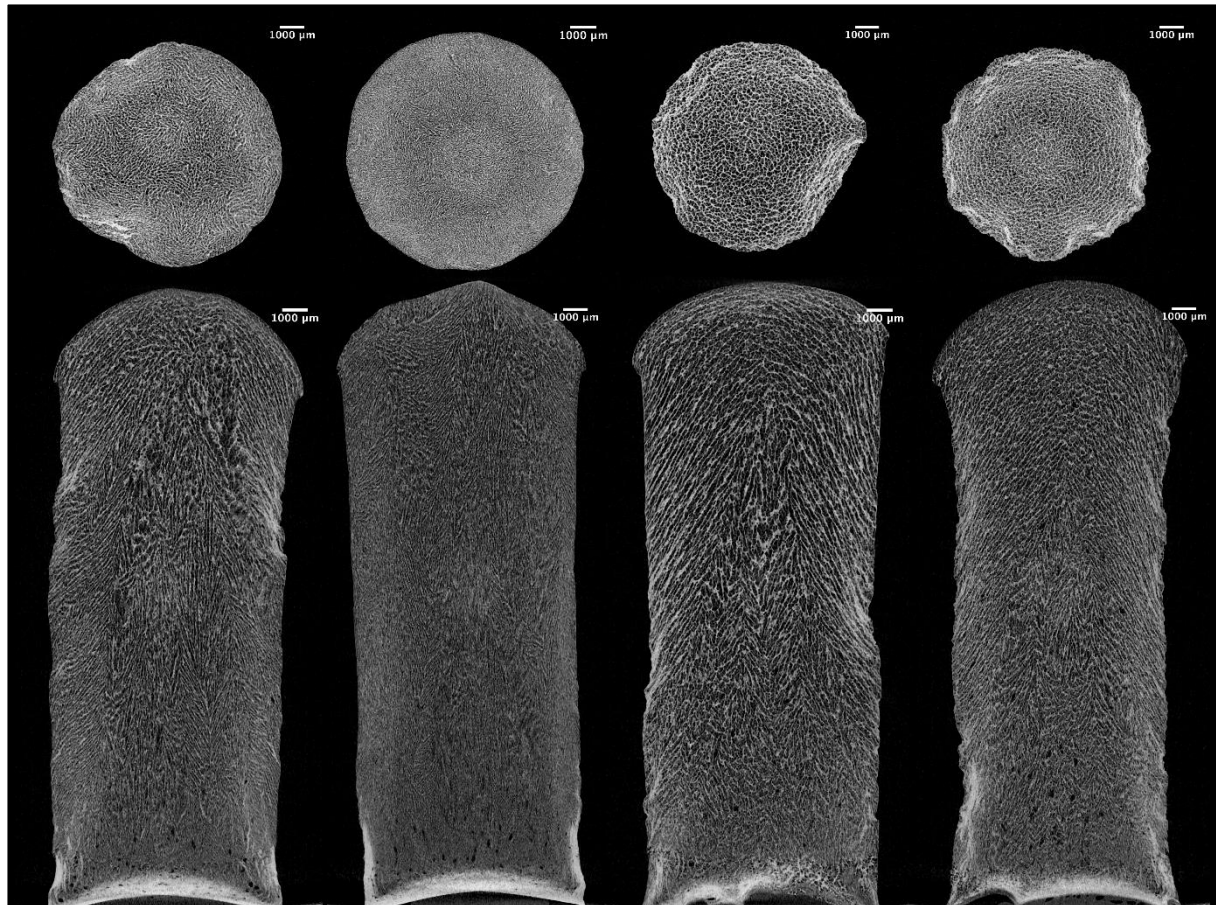


Figure 6. X-ray tomographic cross sections. Top: xy-, bottom: xz-cross planes. From left to right: NG 2 K/min, NG 4 K/min, G 2 K/min, G 4 K/min.

Table 2. Length of the shortest pore axis

Sample	Average [μm]	SD [μm]
NG 2 K/min	77	28
NG 4 K/min	73	245
G 2 K/min	120	47
G 4 K/min	96	43

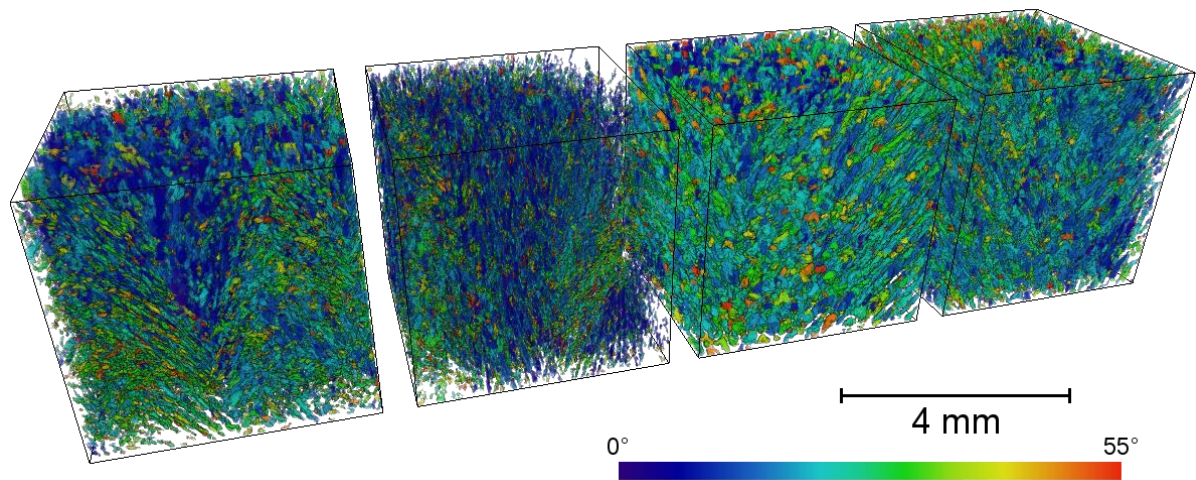
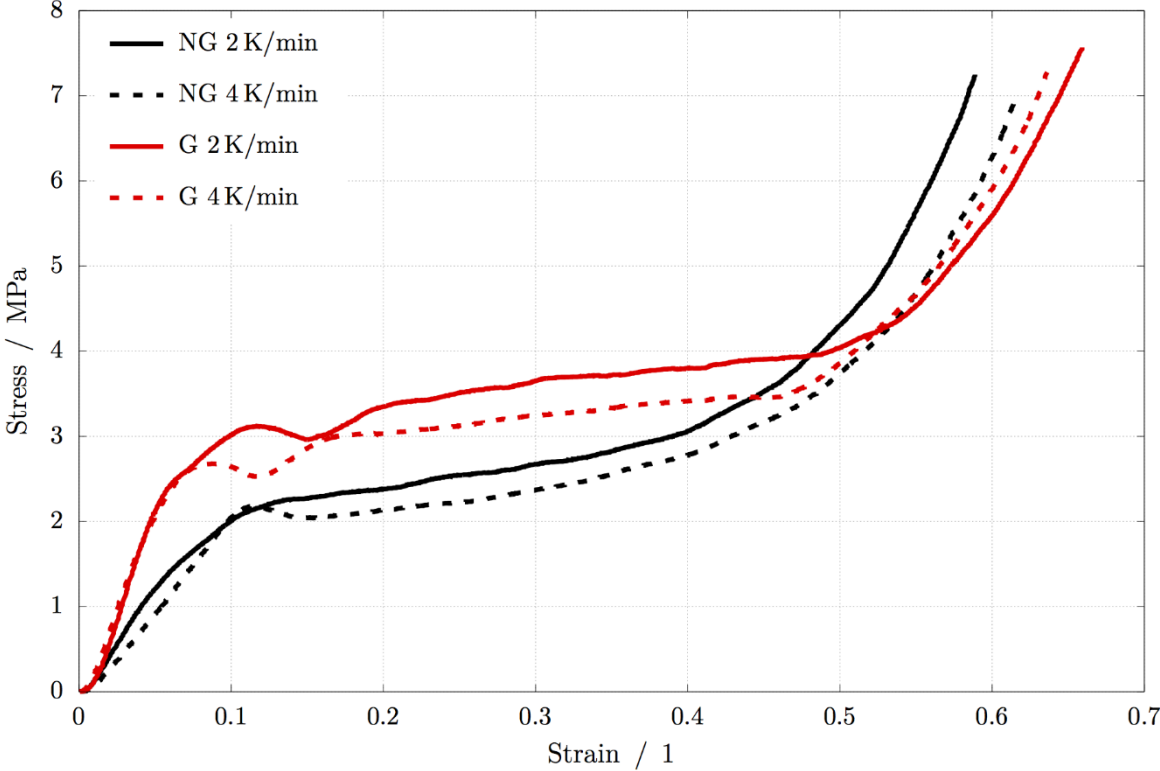


Figure 7. Graphical representation of the angles between the longest pore axis and the freezing direction (0°) obtained from X-ray tomography. From left to right: NG 2 K/min, NG 4 K/min, G 2 K/min, G 4 K/min.

3.3. Mechanical Properties

Figure 8 shows compressive stress-strain diagrams. Since the measured specimens of each group showed similar results, representative graphs are selected. In contrast to ceramics and glasses, which mostly show brittle failure during compression^[52], the shape of the measured curves corresponds to bending-dominated behavior. Up to a certain limit, the samples show a behavior that resembles linear elastic deformation but which might also contain some microplastic deformation after which the edges of a cell fracture under constant stress until the opposing faces of a collapsing cell impinge and the stress continues to increase.^[53] As depicted in **Figure 9**, even after completion of the compressive tests the samples did not fall to pieces. **Table 3** shows the values of the compression strength and quasielastic modulus for each specimen. The quasielastic moduli were ascertained by the slope of the quasilinear graphs in the low-strain part of the stress-strain diagram. While the values of the compressive strength are similar, the G samples exhibit higher quasielastic moduli, exceeding those of NG specimens by a factor of two. The sample G 2 K/min shows the highest mechanical properties of all investigated samples. This can be directly linked to the gelatin network generated during cooling in the fridge before freeze casting of the G samples. Gelation prior to freeze

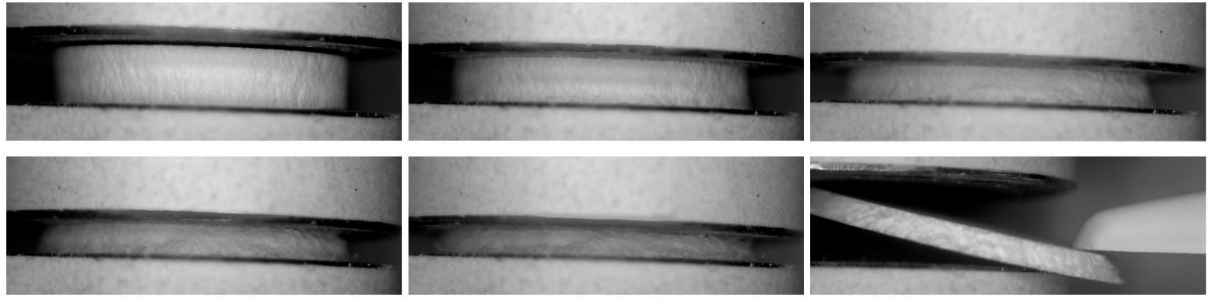
1 casting leads to the formation of a rather cellular pore morphology compared to a more
 2 lamellar pore morphology when the slurry is directly frozen after preparation. During
 3
 4 gelation, interconnections in different directions independent of the previous ice crystal
 5
 6 growth direction occurs.^[54]
 7
 8
 9



10
 11
 12
 13
 14
 15
 16
 17
 18
 19
 20
 21
 22
 23
 24
 25
 26
 27
 28
 29
 30
 31
 32
 33
 34
 35
 36
 37 Figure 8. Stress-strain curves (compression test) of the prepared specimens. The solid and
 38 dotted line represent the freezing rate 2 and 4 K/min, respectively. The black graphs represent
 39 the non-gelled samples, whereas the red ones represent the gelled samples.
 40
 41

42 Table 3. Compression strengths and quasielastic moduli (compression test)

	NG 2 K/min	NG 4 K/min	G 2 K/min	G 4 K/min
Compression strength [MPa]	2.3	2.2	3.1	2.7
Quasielastic modulus [MPa]	19.4	22.7	46.0	44.3



1
2
3
4
5
6
7
8
9
10
11
12
13
14
15
16
17
18
19
20
21
22
23
24
25
26
27
28
29
30
31
32
33
34
35
36
37
38
39
40
41
42
43
44
45
46
47
48
49
50
51
52
53
54
55
56
57
58
59
60
61
62
63
64
65

Figure 9. Digital images showing the rather elastic compression behavior of the samples. The ratio height/diameter is 0.17, the sample depicted is G 2 K/min.

3.4. Bioactivity of the Scaffolds

The bioactivity of the scaffolds was evaluated in an SBF reactor that mimics physiological flow^[48]. After seven days, a calcium phosphate rich layer could be detected on the outside of the scaffolds, see **Figure 10**, implying good bioactivity^[55-57]. After fracturing the sample, the inner parts showed the original chemical composition, as can be seen in the EDX spectra in Figure 10. The calcium (Ca) and phosphorus (P) peaks have a higher intensity for the outer surface of the sample, indicating the formation of a calcium phosphate layer.

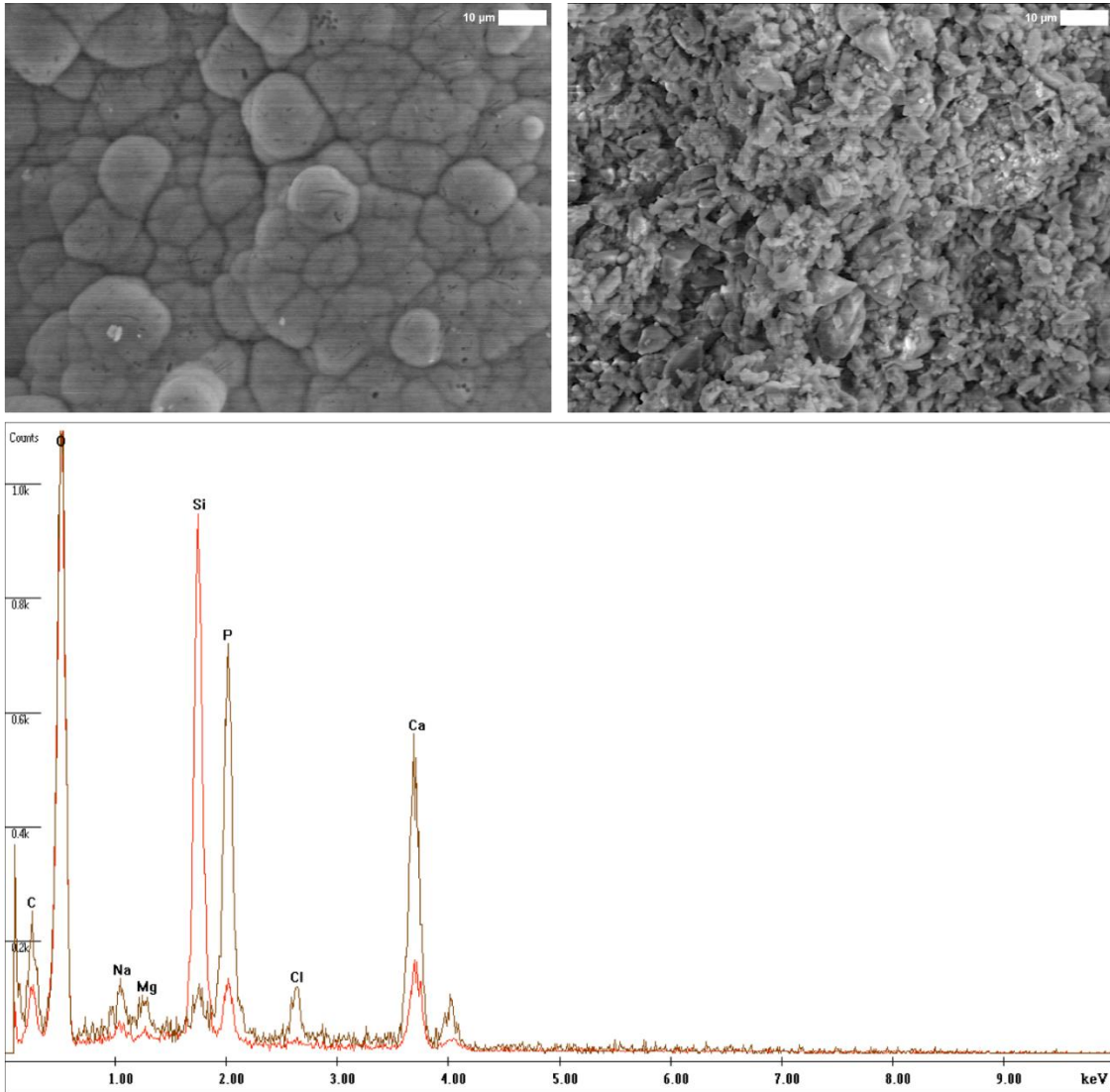


Figure 10. Top: SEM micrographs of NG 4 K/min (thermally treated) after dynamic SBF treatment for seven days (left: surface, right: inside after fraction). Scale bar is 10 μm. Bottom: Corresponding EDX spectra. The brown line corresponds to the surface, the red one to the inside measurement. The developed calcium phosphate rich layer is clearly visible.

4. Conclusions

In this work, we successfully fabricated bioactive macroporous scaffolds with a biopolymer complex via gel casting and freeze casting. By using gelatin and chitosan as binder and stabilizing agent, respectively, for our Bioglass-biopolymer composite scaffolds, we were able to produce highly porous scaffolds with 75 % open porosity.

By varying the processing route of the slurry, meaning not gelling (NG) or gelling (G) the gelatin content prior to freezing, we were able to influence the pore morphology and pore

1 sizes. While the NG samples showed a rather lamellar morphology, the G samples exhibited a
2 more cellular morphology and larger pores. Different freezing rates, namely 2 and 4 K/min,
3 allowed a variation in pore size. The higher freezing rate led to smaller pores, as represented
4 by the length of the shortest pore axis. Gelling of the slurry prior to freezing led to an increase
5 in compressive strength up to 38 % (compare Table 3 samples NG 2 K/min with 2.3 MPa and
6 G 2 K/min with 3.1 MPa). The quasielastic modulus in the G samples was twice as high as in
7 the NG samples. In addition, good bioactivity of the scaffolds could be proven by bioactivity
8 investigations in SBF under physiological flow conditions.
9
10
11
12
13
14
15
16
17
18
19
20
21
22
23
24
25
26
27
28
29
30
31
32
33
34
35
36
37
38
39
40
41
42
43
44
45
46
47
48
49
50
51
52
53
54
55
56
57

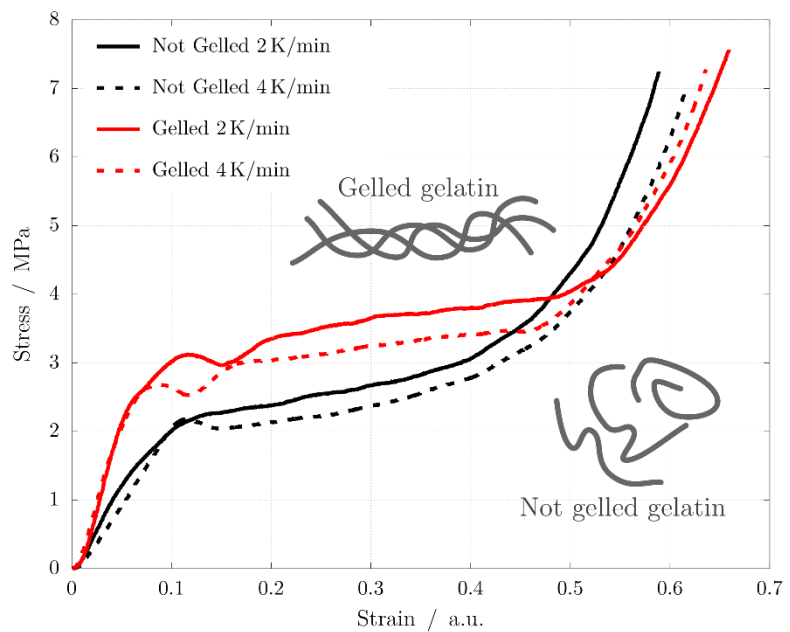
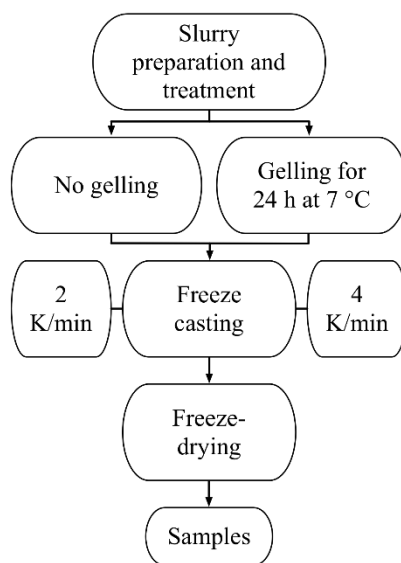
58 Received: ((will be filled in by the editorial staff))
59 Revised: ((will be filled in by the editorial staff))
60 Published online: ((will be filled in by the editorial staff))
61
62
63
64
65

- 1 [1] L. L. Hench, J. M. Polak, *Science* **2002**, 295, 1014.
- 2 [2] J. V. Rau, I. Antoniac, G. Cama, V. S. Komlev, A. Ravaglioli, *Biomed. Res. Int.* **2016**,
- 3 2016, 3741428.
- 4 [3] M. Monleón Pradas, M. J. Vicent (Eds.), *Polymers in regenerative medicine: Biomedical*
- 5 *applications from nano- to macro-structures*, John Wiley & Sons, Inc., Hoboken, New
- 6 Jersey **2015**.
- 7 [4] D. S. Brauer, *Angew. Chem., Int. Ed. Engl.* **2015**, 54, 4160.
- 8 [5] D. S. Brauer, *Angew. Chem.* **2015**, 127, 4232.
- 9 [6] L. L. Hench, *Ann. N. Y. Acad. Sci.* **1988**, 523, 54.
- 10 [7] L. L. Hench, *J. Mater. Sci.:Mater. Med.* **2015**, 26, 86.
- 11 [8] S. Sarin, A. Rekhi, *J. Res. Dent. Sci.* **2016**, 7, 27.
- 12 [9] J. R. Jones, A. G. Clare (Eds.), *Bio-glasses: An introduction*, Wiley, Chichester, West
- 13 Sussex **2012**.
- 14 [10] M. N. Rahaman, D. E. Day, B. S. Bal, Q. Fu, S. B. Jung, L. F. Bonewald, A. P. Tomsia,
- 15 *Acta Biomater.* **2011**, 7, 2355.
- 16 [11] SCHOTT, *SCHOTT Vitryxx® Bioactive Glass: Material data* **2017**,
- 17 [http://www.schott.com/d/epackaging/da339910-2fb7-4c59-a041-](http://www.schott.com/d/epackaging/da339910-2fb7-4c59-a041-4fc1861e8088/1.0/schott-vitryxx-bioactive-glass-material-data-datasheet-eng-2014-06.pdf)
- 18 [4fc1861e8088/1.0/schott-vitryxx-bioactive-glass-material-data-datasheet-eng-2014-](http://www.schott.com/d/epackaging/da339910-2fb7-4c59-a041-4fc1861e8088/1.0/schott-vitryxx-bioactive-glass-material-data-datasheet-eng-2014-06.pdf)
- 19 [06.pdf](http://www.schott.com/d/epackaging/da339910-2fb7-4c59-a041-4fc1861e8088/1.0/schott-vitryxx-bioactive-glass-material-data-datasheet-eng-2014-06.pdf).
- 20 [12] Q. Z. Chen, I. D. Thompson, A. R. Boccaccini, *Biomaterials* **2006**, 27, 2414.
- 21 [13] J. Hum, K. W. Luczynski, P. Noeaid, P. Newby, O. Lahayne, C. Hellmich, A. R.
- 22 Boccaccini, *Strain* **2013**, 49, 431.
- 23 [14] B. Fan, X. Wang, H. Zhang, P. Gao, H. Zhang, X. Li, H. Huang, X. Xiao, D. Liu, Q.
- 24 Lian, Z. Guo, Z. Wang, *Mater. Des.* **2016**, 112, 67.
- 25 [15] Z. Li, N. W. Khun, X.-Z. Tang, E. Liu, K. A. Khor, *J. Mech. Behav. Biomed. Mater.*
- 26 **2017**, 65, 77.
- 27 [16] B. Sarker, W. Li, K. Zheng, R. Detsch, A. R. Boccaccini, *ACS Biomater. Sci. Eng.* **2016**,
- 28 2, 2240.
- 29 [17] J. H. Lopes, J. A. Magalhaes, R. F. Gouveia, C. A. Bertran, M. Motisuke, S. E. A.
- 30 Camargo, E. d. S. Triches, *J. Mech. Behav. Biomed. Mater.* **2016**, 62, 10.
- 31 [18] L. L. Hench, *J. Mater. Sci.: Mater. Med.* **2006**, 17, 967.
- 32 [19] Q. Fu, E. Saiz, M. N. Rahaman, A. P. Tomsia, *Mater. Sci. Eng. C* **2011**, 31, 1245.
- 33 [20] Q. Chen, J. A. Roether, A. R. Boccaccini, *Topics in Tissue Engineering* **2008**, 4, 1.
- 34 [21] K. Whang, K. E. Healy, D. R. Elenz, E. K. Nam, D. C. Tsai, C. H. Thomas, G. W.
- 35 Nuber, F. H. Glorieux, R. Travers, S. M. Sprague, *Tissue Eng.* **1999**, 5, 35.
- 36 [22] B. P. Chan, K. W. Leong, *Eur Spine J* **2008**, 17 (Suppl 4), 467.
- 37 [23] S. Eqtesadi, A. Motealleh, P. Miranda, A. Lemos, A. Rebelo, J. M. Ferreira, *Mater. Lett.*
- 38 **2013**, 93, 68.
- 39 [24] J. G. Dellinger, J. 3. Cesarano, R. D. Jamison, *J. Biomed. Mater. Res. Part A* **2007**, 82,
- 40 383.
- 41 [25] P. Sepulveda, J. G. P. Binner, S. O. Rogero, O. Z. Higa, J. C. Bressiani, *J. Biomed.*
- 42 *Mater. Res.* **2000**, 50, 27-34.
- 43 [26] J. Lacroix, E. Jallot, J. Lao, *Chem. Eng. J.* **2014**, 256, 9.
- 44 [27] M. Mozafari, F. Mozarzadeh, M. Rabiee, M. Azami, S. Maleknia, M. Tahriri, Z.
- 45 Mozarzadeh, N. Nezafati, *Ceram. Int.* **2010**, 36, 2431.
- 46 [28] F. Baino, S. Fiorilli, C. Vitale-Brovarone, *Acta Biomater.* **2016**, 42, 18.
- 47 [29] S. Deville, *Adv. Eng. Mater.* **2008**, 10, 155.
- 48 [30] M. Pourhaghgouy, A. Zamanian (Eds.), *Ice-templated scaffolds of bioglass nanoparticles*
- 49 *reinforced-chitosan*, 21st ICBME **2014**.
- 50 [31] M. Pourhaghgouy, A. Zamanian, M. Shahrezaee, M. P. Masouleh, *Mater. Sci. Eng. C*
- 51 **2016**, 58, 180.
- 52
- 53
- 54
- 55
- 56
- 57
- 58
- 59
- 60
- 61
- 62
- 63
- 64
- 65

- 1 [32] S. Deville, *Materials* **2010**, 3, 1913.
- 2 [33] K. K. Mallick, *J. Am. Ceram. Soc.* **2009**, 92, S85.
- 3 [34] U. G. K. Wegst, M. Schecter, A. E. Donius, P. M. Hunger, *Philos. Trans. R. Soc. A* **2010**,
- 4 368, 2099.
- 5 [35] H. Bai, F. Walsh, B. Gludovatz, B. Delattre, C. Huang, Y. Chen, A. P. Tomsia, R. O.
- 6 Ritchie, *Adv. Mat.* **2016**, 28, 50.
- 7 [36] I. V. Antoniac, *Handbook of bioceramics and biocomposites*, Springer Berlin
- 8 Heidelberg, New York **2016**.
- 9 [37] P. Gentile, M. Mattioli-Belmonte, V. Chiono, C. Ferretti, F. Baino, C. Tonda-Turo, C.
- 10 Vitale-Brovarone, I. Pashkuleva, R. L. Reis, G. Ciardelli, *J. Biomed. Mater. Res. Part A*
- 11 **2012**, 100A, 2654.
- 12 [38] K. Maji, S. Dasgupta, *Trans. Indian Ceram. Soc.* **2016**, 74, 195.
- 13 [39] K. Maji, S. Dasgupta, K. Pramanik, A. Bissoyi, *Int. J. Biomater.* **2016**, 2016, 9825659.
- 14 [40] G. O. Phillips, P. A. Williams (Eds.), *Handbook of food proteins: Gelatin*, Woodhead,
- 15 Oxford **2011**.
- 16 [41] A. Di Martino, M. Sittinger, M. V. Risbud, *Biomaterials* **2005**, 26, 5983.
- 17 [42] I.-Y. Kim, S.-J. Seo, H.-S. Moon, M.-K. Yoo, I.-Y. Park, B.-C. Kim, C.-S. Cho,
- 18 *Biotechnol. Adv.* **2008**, 26, 1.
- 19 [43] S. Deepthi, J. Venkatesan, S.-K. Kim, J. D. Bumgardner, R. Jayakumar, *Int. J. Biol.*
- 20 *Macromol.* **2016**, 93, 1338.
- 21 [44] J. S. Mao, Y. L. Cui, X. H. Wang, Y. Sun, Y. J. Yin, H. M. Zhao, K. D. Yao,
- 22 *Biomaterials* **2004**, 25, 3973.
- 23 [45] L. Lefebvre, J. Chevalier, L. Gremillard, R. Zenati, G. Thollet, D. Bernache-Assolant, A.
- 24 Govin, *Acta Mater.* **2007**, 55, 3305.
- 25 [46] S. Zavareh, A. Hilger, K. Hirslandt, O. Goerke, I. Manke, J. Banhart, A. Gurlo, *J.*
- 26 *Ceram. Soc. Jpn.* **2016**, 124, 1067.
- 27 [47] F. García Moreno, M. Fromme, J. Banhart, *Adv. Eng. Mater.* **2004**, 6, 416.
- 28 [48] M. Höner, F. Boke, M. Weber, H. Fischer, *J. Biomed. Mater. Res. Part B* **2017**, article in
- 29 *press*.
- 30 [49] S. Lopez-Esteban, E. Saiz, S. Fujino, T. Oku, K. Suganuma, A. P. Tomsia, *J. Eur.*
- 31 *Ceram. Soc.* **2003**, 23, 2921.
- 32 [50] L.-C. Gerhardt, A. R. Boccaccini, *Materials* **2010**, 3, 3867.
- 33 [51] A. F. Recum, C. E. Shannon, C. E. Cannon, K. J. Long, T. G. Kooten, J. Meyle, *Tissue*
- 34 *Eng.* **1996**, 2, 241.
- 35 [52] A. J. Salinas, M. Vallet-Regí, *RSC Adv.* **2013**, 3, 11116.
- 36 [53] M. Scheffler, P. Colombo, *Cellular ceramics: Structure, manufacturing, properties and*
- 37 *applications*, Wiley-VCH; Chichester, Weinheim **2005**.
- 38 [54] D. Zhang, Y. Zhang, R. Xie, K. Zhou, *Ceram. Int.* **2012**, 38, 6063.
- 39 [55] T. Kokubo, H. Takadama, *Biomaterials* **2006**, 27, 2907.
- 40 [56] L. L. Hench, R. J. Splinter, W. C. Allen, T. K. Greenlee, *J. Biomed. Mater. Res.* **1971**, 5,
- 41 117.
- 42 [57] S. Fujibayashi, *Biomaterials* **2003**, 24, 1349.
- 43
- 44
- 45
- 46
- 47
- 48
- 49
- 50
- 51
- 52
- 53
- 54
- 55
- 56
- 57
- 58
- 59
- 60
- 61
- 62
- 63
- 64
- 65

Table of Contents

The combination of gel casting and freeze casting results in better mechanical properties compared to the sole use of the conventional freeze casting technique. Highly porous 45S5 Bioglass/gelatin/chitosan composite scaffolds which were gel casted before freeze casting, show an increase in the quasielastic moduli by 100 % and sufficient pore sizes for applications in bone tissue engineering.



List of Figures

1		
2	Figure 1. Scheme depicting the experimental procedure for the scaffold production	4
3	Figure 2. From left to right: Typical image of a sample, schematic for the geometrical	
4	approximation, X-ray tomography reconstruction (G 2 K/min) showing the analyzed volume.	
5	6
6	Figure 3. The particle size distribution of the Bioglass powder and the prepared slurry.	
7	Black/filled symbols and gray/hollow symbols illustrate the cumulative distribution and	
8	distribution density over particle size, respectively.	9
9	Figure 4. The dynamic viscosity of the slurry decreases with an increasing shear rate	
10	confirming the shear-thinning behavior of the slurry. Black/filled symbols and gray/hollow	
11	symbole illustrate the dynamic viscosity and shear stress over shear rate, respectively.....	10
12	Figure 5. SEM micrographs of the prepared scaffolds. Top left: NG 2 K/min, bottom left:	
13	NG 4 K/min, top right: G 2 K/min, bottom right: G 4 K/min. Scale bar is 90 μm	11
14	Figure 6. X-ray tomographic cross sections. Top: xy-, bottom: xz-cross planes. From left to	
15	right: NG 2 K/min, NG 4 K/min, G 2 K/min, G 4 K/min.	13
16	Figure 7. Graphical representation of the angles between the longest pore axis and the	
17	freezing direction (0°) obtained from X-ray tomography. From left to right: NG 2 K/min,	
18	NG 4 K/min, G 2 K/min, G 4 K/min.....	14
19	Figure 8. Stress-strain curves (compression test) of the prepared specimens. The solid and	
20	dotted line represent the freezing rate 2 and 4 K/min, respectively. The black graphs represent	
21	the non-gelled samples, whereas the red ones represent the gelled samples.	15
22	Figure 9. Digital images showing the rather elastic compression behavior of the samples. The	
23	ratio height/diameter is 0.17, the sample depicted is G 2 K/min.	16
24		
25		
26		
27		
28		
29		
30		
31		
32		

List of Tables

33		
34		
35	Table 1. Solid densities, raw densities and calculated porosities of all specimens.....	10
36	Table 2. Length of the shortest pore axis	13
37	Table 3. Compression strengths and quasielastic moduli (compression test)	15
38		
39		
40		
41		
42		
43		
44		
45		
46		
47		
48		
49		
50		
51		
52		
53		
54		
55		
56		
57		
58		
59		
60		
61		
62		
63		
64		
65		